Rational design of highly selective nitrogen-doped Fe$_2$O$_3$-CNTs catalyst towards H$_2$O$_2$ generation in alkaline media

Xiaoyang Cheng [a,1], Shasha Dou [a,1], Guihua Qin [a], Benzhi Wang [a], Puxuan Yan [a], Tayirjan Taylor Isimjan [b,**], Xiulin Yang [a,*]

[a] Guangxi Key Laboratory of Low Carbon Energy Materials, School of Chemistry and Pharmaceutical Sciences, Guangxi Normal University, Guilin, 541004, People's Republic of China
[b] Saudi Arabia Basic Industries Corporation (SABIC) at King Abdullah University of Science and Technology (KAUST), Thuwal, 23955-6900, Saudi Arabia

HIGHLIGHTS

- Nitrogen-doped carbon wrapped Fe$_2$O$_3$-CNTs composite is synthesized by a facile and controllable method.
- The NC@Fe$_2$O$_3$-CNTs catalyst exhibits high activity, selectivity and long term stability on ORR for H$_2$O$_2$ generation.
- A synergistic effect between the N-doped carbon and Fe$_2$O$_3$ clusters is proved to dominate the superior catalytic performance.
- A reasonable catalytic mechanism is proposed based on experimental results.

GRAPHICAL ABSTRACT
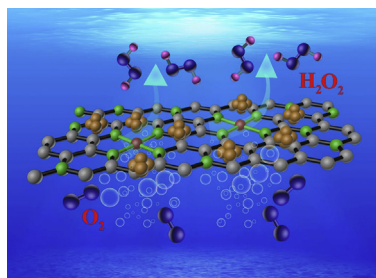
ARTICLE INFO

ABSTRACT

The continuous on-site production of H$_2$O$_2$ using an inexpensive metal catalyst based electrochemical approach as the alternative of the widely used complex anthraquinone process is particularly promising. Although tremendous progress has been made in recent years towards developing oxygen reduction reaction (ORR) catalyst for H$_2$O$_2$ production, fabricating highly active, selective, and stable H$_2$O$_2$ catalyst that works at high pH is always the challenge. Here, we describe a rationally designed non-precious metal-based nitrogen-doped Fe$_2$O$_3$-carbon nanotubes (NC@Fe$_2$O$_3$-CNTs) catalyst, which not only exhibits high ORR activity and low overpotential but also shows a unique selectivity towards H$_2$O$_2$ generation (97.3%) in alkaline media. Moreover, the NC@Fe$_2$O$_3$-CNTs catalyst retains a

* Corresponding author.
** Corresponding author.
    E-mail addresses: isimjant@sabic.com (T.T. Isimjan), xlyang@gxnu.edu.cn (X. Yang).
[1] These authors contributed equally.

Fe$_2$O$_3$ clusters
Nitrogen-doped
Oxygen reduction
Hydrogen peroxide

much higher relative current after continuous operation for 10 h, as compared to commercial Pt/C catalyst. The optimized NC@Fe$_2$O$_3$-CNTs shows the superior overall performance of H$_2$O$_2$ generation as compared to the present catalysts under high pH. The catalytic mechanism analysis indicates that the nitrogen species, Fe chemical states, oxygen vacancies and CNTs skeleton play important roles in improving the selectivity and current density of H$_2$O$_2$ generation.

Introduction

Hydrogen peroxide (H$_2$O$_2$) is an eco-friendly oxidant widely utilized for chemical synthesis and environmental remediation [1,2]. The remarkable oxidation properties of hydrogen peroxide allow various oxidizing chemicals, including the organic pollutants in the water stream. More than 95% of H$_2$O$_2$ is produced through the energy-intensive anthraquinone oxidation process today [3]. However, the anthraquinone oxidation process requires an enormous infrastructure, a large amount of hydrogen, and a high quantity of organic solvent. Besides, it involves stabilizers for preventing degradation of anthraquinone molecules and H$_2$O$_2$. Moreover, the unstable nature of H$_2$O$_2$ makes long-distance transport very challenging and limits the accessibility of H$_2$O$_2$ in remote rural areas [4]. Hence, the continuous on-site production of H$_2$O$_2$ using an inexpensive metal catalyst based electrochemical reduction approach that follows a two-electron pathway is a promising alternative. However, the two-electron processes often accompany by a four-electron path that generates H$_2$O [2]. As a result, designing an ORR catalyst with high selectivity towards the two-electron pathway is the critical step on the way to obtaining a high-performance H$_2$O$_2$ catalyst. However, mostly noble metals based ORR catalysts can meet all those requirements [5].

Recently, the carbon-based materials have shown promising performances because of the large surface areas, low cost, high electrical conductivity, highly tenability, and electrochemical stability [6–8]. Studies demonstrated that the performance of the carbon material based electrochemical H$_2$O$_2$, the catalyst, can be optimized by tailoring the electronic property by changing the catalyst morphology and doping foreign atoms [8]. The other factor that affects the overall catalyst performance is the pH of the reaction media. In general, the natural or basic pH is preferred over the acid pH due to the acidic corrosion. However, some studies revealed that H$_2$O$_2$ becomes less stable in alkaline conditions, especially at pH > 9 [9]. The main problems of the conventional nonprecious metal catalysts [10–12] are that they show high performance in H$_2$O$_2$ production under acidic condition but favor the four-electron pathway under alkaline condition [13–15]. Because the transition-metal based active sites prefer for four-electron reduction in high pH [16–18]. Therefore, most of the precious metals or heteroatom-doped carbon materials show either low current density or low selectivity at high pH.

Herein, we designed a simple method of synthesizing NC@Fe$_2$O$_3$-CNTs composite by in-situ pyrrole polymerization on the surface of organometallic frameworks (MOF). Electrochemical studies revealed that the optimized NC@Fe$_2$O$_3$-CNTs catalyst exhibits excellent catalytic performance for electrochemical reduction of O$_2$ to H$_2$O$_2$ in alkaline media. The maximum limiting current density and the corresponding selectivity of H$_2$O$_2$ are −5.96 mA cm-2 at 0.2 V and 97.3%, respectively, which are much higher than those reported in the literature (Table S2). For example, The H$_2$O$_2$ catalyst with the highest selectivity under alkaline media reported so far is N-doped C is 93% (Table S2). Although the N-doped C revealed the same current density as NC@Fe$_2$O$_3$-CNTs, the catalyst loading and overpotential are much higher than those of NC@Fe$_2$O$_3$-CNTs as shown in Table S2. Moreover, the optimized NC@Fe$_2$O$_3$-CNTs catalyst shows strong resistance to catalyst poisoning; therefore, it displays high stability. The crystal structure, specific surface area, metal oxide content, nitrogen content, elemental state, and microstructure of the series of the catalysts were analyzed by XRD, Raman, BET, TG-DTG, elemental analyzer, XPS, SEM and TEM method. The oxygen reduction reaction (ORR) of the 2-electron transfer process described by the Koutecky-Levich (K-L) equation was also confirmed by the rotating ring-disk electrode (RRDE) test. Finally, a possible reaction mechanism is proposed.

Experimental section

Synthesis of MIL-101-Fe crystals

The MIL-101-Fe crystals were obtained according to the reported procedure with minor modifications. Initially, 4.0 mmol of FeCl$_3$ and 4.0 mmol of H$_2$BDC were ultrasonically dissolved into 40 mL of N,N-dimethylformamide (DMF) for 5 min. After stirring for another 10 min, the resulted solution was slowly heated to 100 °C for 12 h in an oil bath, and then naturally cooled down to room temperature. After centrifugation, abundant ethanol washing and vacuum drying overnight, an orange powder was obtained. The as-received powders are nominated as MIL-101-Fe crystals.

Synthesis of NC@Fe$_2$O$_3$-CNTs composite

The series of N-doped carbon coated Fe$_2$O$_3$-CNTs (NC@Fe$_2$O$_3$-CNTs) were prepared as below. Firstly, 0.3 g of MIL-101-Fe crystals and 0.060 g of carbon nanotubes (CNTs) were dispersed in 50 mL of deionized (DI) water under vigorously stirring. Ten minutes later, 2 mL of pyrrole was pipetted into the above solution and the resulted mixture was continuously stirring for 30 min. Subsequently, 50 mL of 11.6 mM

ammonium persulfate (APS) solution was slowly added dropwise into the above mixtures under continuous stirring at room temperature. After uninterruptedly stirring for another 12 h, the product of polypyrrole@MIL-101-Fe-CNTs was separated by filtration coped with abundant H_2O and ethanol washing. After being freeze-dried, the resulted powder was placed in a tube furnace, slowly raised to different temperatures (700, 800, and 900 °C) with a heating rate of 5 °C min^{-1} in an Ar atmosphere, and maintained at the same temperature for 3 h. Note: Unless otherwise specified, NC@Fe$_2$O$_3$-CNTs refers to an 800 °C calcined product in this work.

As for comparison, the NC@Fe$_2$O$_3$, NC@CNTs and Fe$_2$O$_3$-CNTs were also prepared by carbonizing the precursors of Ppy@MIL-101-Fe, Ppy@CNTs, and MIL-101-Fe-CNTs at 800 °C in Ar atmosphere, respectively.

Electrochemical measurements

The ORR activities of the as-prepared catalysts were studied by an electrochemical workstation of Biologic VMP3 with a typical three-electrode system in N_2- or O_2-saturated 0.1 M KOH electrolyte. A rotating disk (glassy carbon, GC) electrode with a diameter of 4 mm, graphite plate and Ag/AgCl electrode were used as working, counter, and reference electrodes, respectively. The GC electrodes were polished with aluminum powder, and then cleaned in sulfuric acid, ethanol, and water subsequently for three times before use. The working electrode was prepared as follows: 2 mg of the as-synthesized catalyst powder was ultrasonically dispersed into 400 μL (V_{water}:$V_{2-propanol}$:V_{Nafion} = 4:1:0.025) aqueous solution. Thirty minutes later, 10 μL of the catalyst inks were pipetted onto several GC electrodes and dried at room temperature. The loading of the catalyst on GC electrode is *ca.* 0.4 mg cm^{-2}. It should be noted that commercial Pt/C (20 wt%) modified GC electrodes adopt a similar method as above, in which 5 μL of Pt/C inks is pipetted onto GC surface with a loading of 0.2 mg cm^{-2}.

The cyclic voltammograms (CV) measurements were recorded in N_2- or O_2-saturated 0.1 M KOH electrolyte with a scan rate of 50 mV s^{-1}. The linear sweep voltammetry (LSV) curves were conducted at a scan rate of 10 mV s^{-1} with a rotating speed from 400 to 2500 rpm in O_2-saturated 0.1 M KOH. The chronoamperometric curves were operated at a constant potential of 0.56 V (vs. RHE) in O_2-saturated 0.1 M KOH. All potentials (vs. Ag/AgCl) in this work were calibrated to the RHE by the average CV curves of the two potentials at which the current crossed zero (0.960 V) was taken to be the thermodynamic potential in H_2-saturated 0.1 M KOH (Fig. S1). All curves were reported here without iR compensation, and all the electrochemical tests were performed at room temperature (25 ± 1 °C).

Results and discussion

Synthetic strategy analysis

The synthesis of NC@Fe$_2$O$_3$-CNTs is shown in Scheme 1, where the CNTs, MIL-101-Fe, and pyrrole monomer are initially well-mixed by vigorously stirring in aqueous solution.

As the strong oxidizing agent of APS is slowly added, the uniformly dispersed pyrrole monomer slowly polymerizes on the surface of MIL-101-Fe-CNTs to form Ppy@MIL-101-Fe-CNTs composite. After carbonization at 800 °C in the Ar atmosphere, the Ppy was converted into a uniformly coated protection layer on the surface of the MIL-101-Fe, which was turned into a three-dimensional skeleton that comprised of Fe$_2$O$_3$ nanoclusters. A good ORR performance is expected through their synergistic effect. It is worth mentioning that introducing CNTs can increase the electrical conductivity of the composite materials substantially. Besides, a series of control materials were prepared (NC@Fe$_2$O$_3$, NC@CNTs, and Fe$_2$O$_3$-CNTs), in order to further investigate the effect of each component on catalytic performance.

Crystal structures, compositions and thermal studies

The crystal structures of the synthesized NC@Fe$_2$O$_3$-CNTs together with Fe$_2$O$_3$-CNTs were characterized by XRD (Fig. 1a). The NC@Fe$_2$O$_3$-CNTs exhibits the typical diffraction peaks of γ-Fe$_2$O$_3$ (JCPDS: 39−1346), as well as a sharp peak at *ca.* 25.8° representing (002) plane of graphitic carbon [19,20]. The similar diffraction peaks were simultaneously observed on the calcined materials at 700 and 900 °C (Fig. S2a). It was worth noting that the Fe$_2$O$_3$-CNTs (Fig. S2b) not only shows the Fe$_2$O$_3$ diffraction peaks but also reveals two distinctive diffraction peaks at 47.6° and 51.9° representing the (600) and (402) planes of Fe$_5$C$_2$ (JCPDS: 20−0508) respectively. The Fe$_5$C$_2$ species in Fe$_2$O$_3$-CNTs could be caused by carbon doping at high temperature, indicating the demolition of the NC-protective layers [21]. The degree of graphitization of the composites is calculated by Raman using the intensity ratio (I_D/I_G) of the disorder-induced D-band (sp^3 carbon) and graphitic G-band (sp^2 carbon) [22]. Fig. 1b showed that the intensity ratio of NC@Fe$_2$O$_3$-CNTs was 0.88, slightly lower than that of NC@Fe$_2$O$_3$-CNTs obtained at 700 °C (0.90) and 900 °C (1.11) as well as some other control samples (Fig. S3), indicating a higher degree of graphitization after calcined at 800 °C. The higher graphitization property means higher conductivity and corrosion resistance in the electrocatalytic process [23]. In this regard, the 800 °C is found to be the optimal annealing temperature.

The specific surface area and the porosity of NC@Fe$_2$O$_3$-CNTs are also investigated by Brunauer-Emmett-Teller (BET) gas-sorption measurements (Fig. 1c). The N_2 adsorption-desorption isotherms at 77 K shows a type IV isotherm with a distinct hysteresis loop at relative pressures (P/P$_o$) of *ca.* 0.3 to 1.0. The BET, specific surface area of NC@Fe$_2$O$_3$-CNTs, is *ca.* 224.0 m^2 g^{-1} (Fig. 1c), and the pore size distribution, calculated by the Barrett-Joyner-Halenda (BJH) method, are mainly centered at *ca.* 13.8 and 23.8 nm (inset of Fig. 1c). The unique hierarchical mesoporous material not only facilitates electrolyte transportation and O_2 diffusion but also exposes more active sites to improve ORR kinetics [24−26].

The mass content of Fe$_2$O$_3$ nanoclusters in NC@Fe$_2$O$_3$-CNTs is evaluated by TG and DTG curves (Fig. 1d). A slight decrease below 125 °C is due to the evaporation of moisture. The two distinct exothermic peaks at 432 and 534 °C in the range of 36−800 °C associated with the combustion of amorphous carbon and crystalline carbon, respectively [27,28]. The total weight loss of *ca.* 87.4 wt % indicating the mass content of
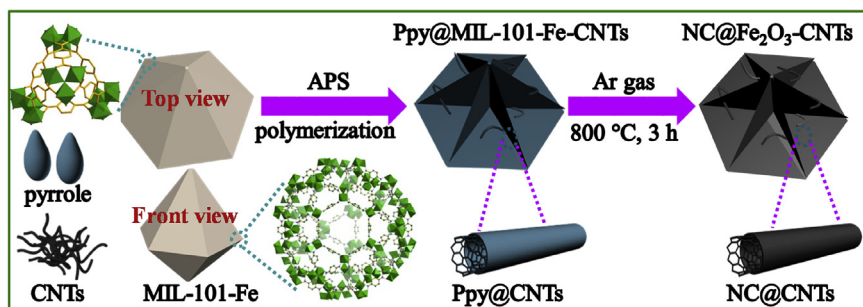
Scheme 1 — Schematic illustration of the reaction process for synthesizing NC@Fe$_2$O$_3$-CNTs.

Fe$_2$O$_3$ species in the hybrid catalyst, is *ca.* 12.6 wt %. Moreover, the N content in the carbonized samples at different temperatures was analyzed by an elemental analyzer. As expected, the total N content progressively decreases with the increase of the carbonization temperatures, as reported in the literature (Table S1) [13,29].

Microstructures analysis

The morphologies and microstructures of the MIL-101-Fe, Ppy@MIL-101-Fe-CNTs, and NC@Fe$_2$O$_3$-CNTs are characterized by scanning electron microscopy (SEM) and transmission electron microscopy (TEM). The MIL-101-Fe crystals present well-defined dodecahedron metal-organic-frameworks (MOF) with a smooth surface and a uniform particle size of *ca.* 1.0 μm (Fig. 2a). After the polymerization of the pyrrole monomer, the resulted Ppy@MIL-101-Fe-CNTs exhibits three-dimensional sheet-like assembled structures (Fig. 2b), which are formed by the dissolution-reassembly process of MOF in aqueous

solution [30]. After calcination at 800 °C in Ar atmosphere, the morphology of NC@Fe$_2$O$_3$-CNTs was basically unchanged (Fig. 2c). The TEM images are further used to study the change migration in microstructures. It was observed that the MIL-101-Fe shows solidly rhombic structure (Fig. 2d), and the Ppy@MIL-101-Fe-CNTs appears to be a porous lamellar structure in the selected domain (Fig. 2e). After calcination, the microstructure of NC@Fe$_2$O$_3$-CNTs changes very little (Fig. 2f) as compared to that of the control samples (Ppy@MIL-101-Fe and Ppy@CNTs) (Fig. S4). A similar structural reorganization is observed in the Ppy@MIL-101-Fe composite. Additionally, the high-resolution TEM image (Fig. 2g) of NC@Fe$_2$O$_3$-CNTs confirms the cubic phase of Fe$_2$O$_3$ clusters with the distinctly periodic lattice fringes, which is the single crystal of γ-Fe$_2$O$_3$. The d-spacing of 0.48 nm can be indexed to (111) planes. Moreover, a thin layer of N-doped carbon (2.92 nm) covers the surface of Fe$_2$O$_3$ crystals. The N-doped carbon layer not only inhibits the agglomeration of Fe$_2$O$_3$ clusters but also generating Fe-N$_x$ active sites at the interface. These are the
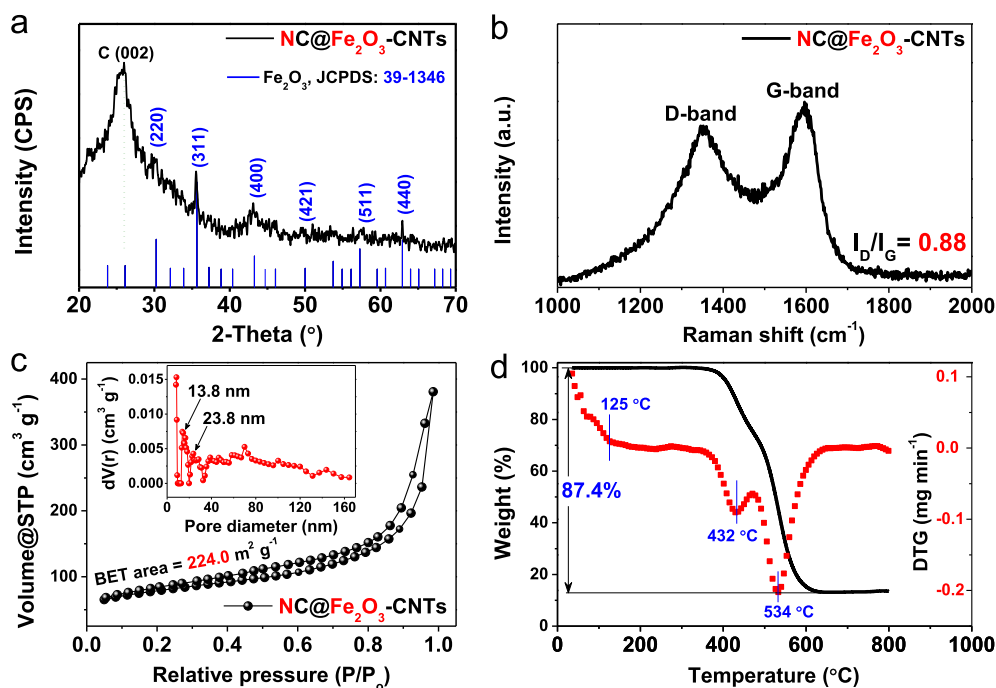
Fig. 1 — (a) X-ray diffraction (XRD) patterns, (b) Raman spectrum, (c) Nitrogen adsorption−desorption isotherms with the pore size distribution curves by the BJH method (inset), and (d) Thermal gravimetric (TG) analysis and derivative thermal gravimetric (DTG) curves of NC@Fe$_2$O$_3$-CNTs in O$_2$ atmosphere with a rising temperature rate of 2.5 °C min^{-1}.
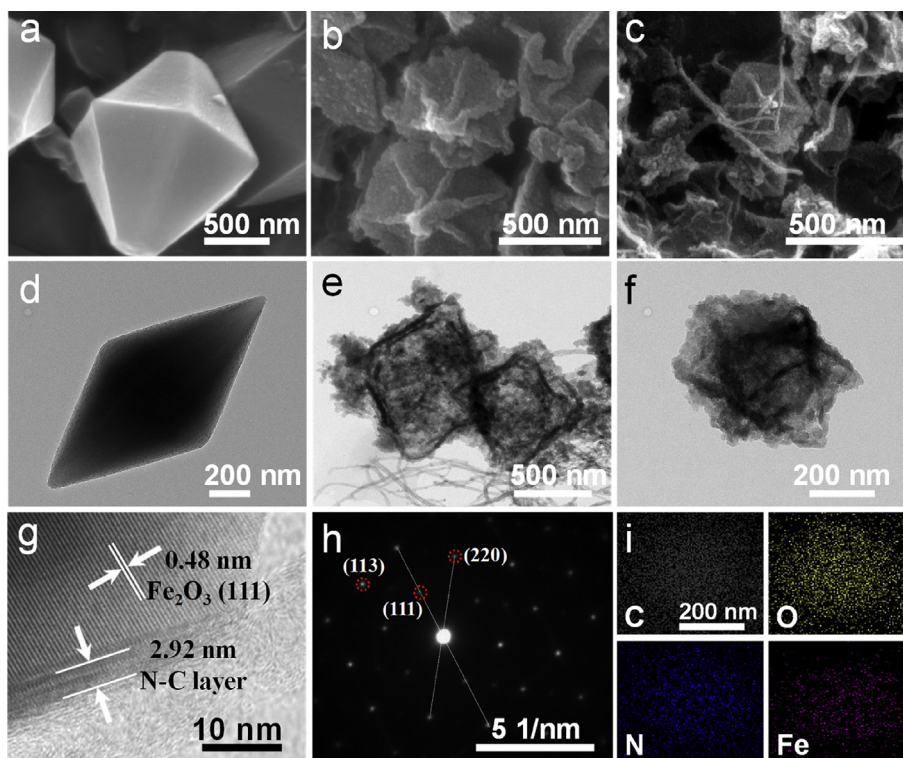
Fig. 2 – SEM images of (a) MIL-101-Fe crystals, (b) Ppy@MIL-101-Fe-CNTs and (c) NC@Fe$_2$O$_3$-CNTs. TEM images of (d) MIL-101-Fe crystals, (e) Ppy@MIL-101-Fe-CNTs and (f) NC@Fe$_2$O$_3$-CNTs. (g) High-resolution TEM image, (h) SAED pattern and (i) HAADF-STEM image and its corresponding elemental mappings of NC@Fe$_2$O$_3$-CNTs.

distinctive futures of efficient catalysts [31]. The electron diffraction (SAED) of the selected-area (Fig. 2h) confirms the phase of γ-Fe$_2$O$_3$ with a [1$\bar{1}$0] zone axis. Element mapping demonstrates that the elements of C, O, N, and Fe are uniformly dispersed throughout the entire architectures of the NC@Fe$_2$O$_3$-CNTs (Fig. 2i).

Electrochemical analysis

Cyclic voltammetry measurements first evaluated the electrocatalytic activities of NC@Fe$_2$O$_3$-CNTs toward the ORR. The experiment was performed in both N$_2$- and O$_2$-saturated 0.1 M KOH solution at a scan rate of 50 mV s^{-1}. There is no distinctive redox peak in the N$_2$-saturated solution, whereas there is a well-defined cathodic peak at 0.83 V in O$_2$-saturated electrolytes (Fig. 3a), indicating a good ORR catalytic activity of the NC@Fe$_2$O$_3$-CNTs [32]. The LSV curves of temperature effect on NC@Fe$_2$O$_3$-CNTs catalysts are further explored in Fig. 3b. The onset potentials of series NC@Fe$_2$O$_3$-CNTs catalysts display a gradual negative shift with increasing calcination temperatures, whereas the synthesized NC@Fe$_2$O$_3$-CNTs at 800 °C shows the maximum limiting current density. As shown in Figs. S5–S7, the LSV polarization curves show that the current densities increase with increasing rotation speeds due to the thin diffusion layer at a high rotation speed, which subsequently results in better O$_2$ permeability. The corresponding Koutecky-Levich (K-L) plots demonstrate significantly different electron transfer numbers ranging from 2.0 to 3.2 because of the high limiting current density and high faradaic efficiency. Accordingly, the NC@Fe$_2$O$_3$-CNTs catalyst

calcined at 800 °C is selected for further study. As shown in Fig. 3c, LSV measurements investigated the ORR catalytic activities of the catalysts calcined at 800 °C with a scan rate of 5 mV s^{-1}. The NC@Fe$_2$O$_3$-CNTs catalyst exhibits the highest ORR activity with a positive onset potential (E$_{onset}$) of 0.96 V and the half-wave potential (E$_{1/2}$) of 0.84 V in 0.1 M KOH. The NC@Fe$_2$O$_3$-CNTs shows the maximum limiting current density (5.96 mA cm^{-2}) at 0.2 V, which is *ca.* 1.25−, 1.76−, 1.12− and 1.17−fold higher than that of NC@CNTs, Fe$_2$O$_3$-CNTs, NC@CNTs, and commercial Pt/C respectively. The excellent catalytic activity of the NC@Fe$_2$O$_3$-CNTs is due to the synergic effect between N-doped carbon, Fe$_2$O$_3$ species, and CNTs. The corresponding electron transfer numbers of different catalysts are summarized in Fig. 3d obtained from the rotation speeds dependent LSV curves (Fig. S8). All the curves are fitted linearly by K-L plots representing the first-order reaction kinetics [33]. We can find that the electron transfer numbers of NC@Fe$_2$O$_3$-CNTs, NC@Fe$_2$O$_3$, and NC@CNTs are similar (close to 2.0). However, the electron transfer number of Fe$_2$O$_3$-CNTs is *ca.* 3.5, and commercial Pt/C is *ca.* 4.0, respectively, indicating the importance of the N-doped carbon encapsulation in the 2e$^-$ transfer process. The 2e$^-$ transfer process is demonstrated by RRDE measurements (Fig. S9). As the current density of the NC@Fe$_2$O$_3$-CNTs catalyst increases, the oxidation current of the ring electrode also increases synchronously, while the ring current of the Fe$_2$O$_3$-CNTs catalyst does not change much (Fig. 3e). The selectivity of H$_2$O$_2$ on NC@Fe$_2$O$_3$-CNTs catalyst is calculated, and the results are ranging from 93.7% to 97.3% which are significantly higher than that of Fe$_2$O$_3$-CNTs (25.4%−36.1%) in the potential range of 0.2−0.6 V
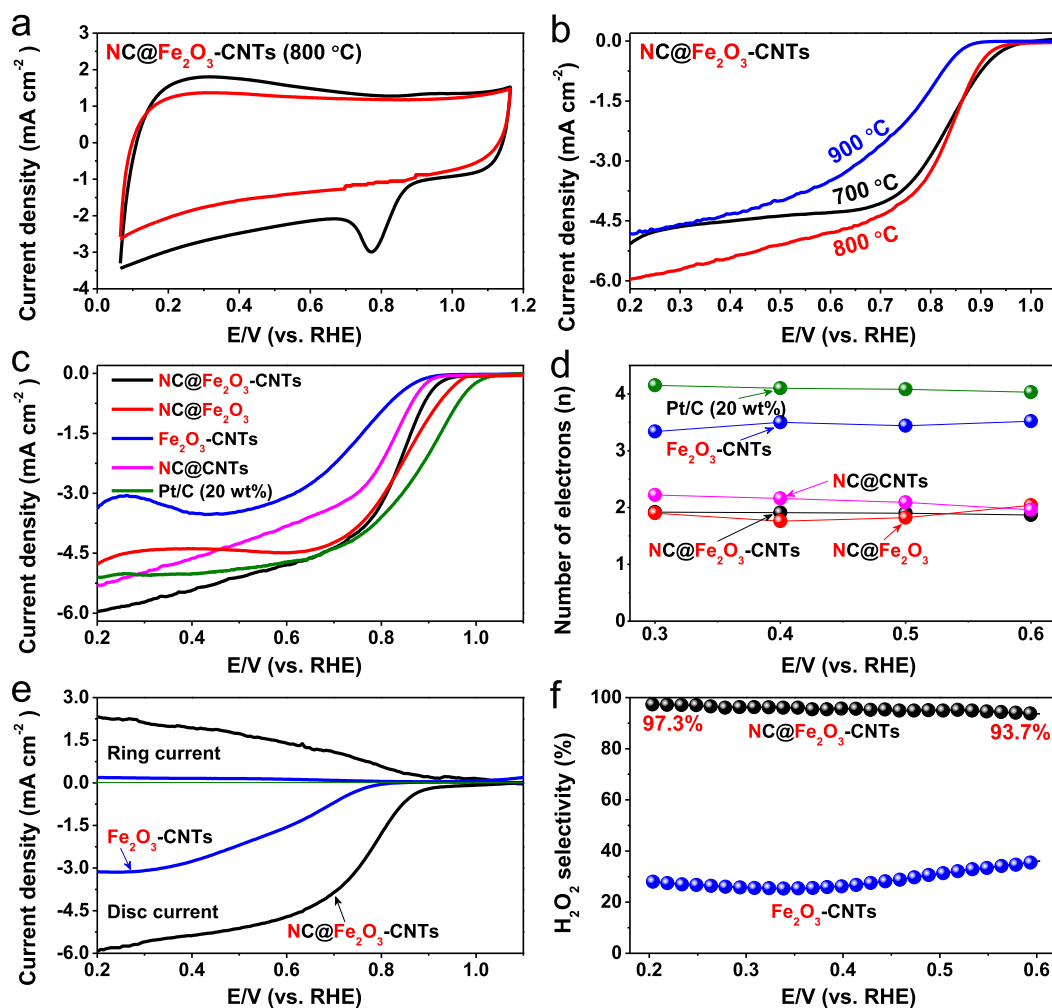
Fig. 3 – (a) CV curves of NC@Fe$_2$O$_3$-CNTs catalyst in 0.1 M KOH solution saturated by N$_2$ or O$_2$. (b) LSV curves of NC@Fe$_2$O$_3$-CNTs catalysts calcined at different temperatures at 1600 rpm in O$_2$-saturated 0.1 M KOH solution. (c) LSV curves and (d) corresponding summarized electron transfer numbers of different catalysts (800 °C calcination) at 1600 rpm in O$_2$-saturated 0.1 M KOH solution. (e) RRDE voltammograms with the ring current corresponding to H$_2$O$_2$ oxidation obtained from the disc current and (f) corresponding H$_2$O$_2$ selectivity as a function of applied potentials of NC@Fe$_2$O$_3$-CNTs and Fe$_2$O$_3$-CNTs catalysts at 1600 rpm in O$_2$-saturated 0.1 M KOH electrolyte.

(Fig. 3f). That is consistent with the results from K−L plots. The ultra-high current density and H$_2$O$_2$ selectivity are far better than those of previously reported materials (Table S2), demonstrating a great industrial application prospect.

The number of active sites is usually proportional to the electrochemical double-layer capacitances (C$_{dl}$) [34]. The C$_{dl}$ of all catalysts is measured by scan-rate dependent CV measurement within a non-Faradaic region in 0.1 M KOH (Fig. 4a and Fig. S10). As shown in Fig. 4b, the calculated C$_{dl}$ values of NC@Fe$_2$O$_3$-CNTs is determined to be 2.59 mF cm^{-2}, much higher than those of NC@Fe$_2$O$_3$ (1.52 mF cm^{-2}), NC@CNTs (0.43 mF cm^{-2}) and Fe$_2$O$_3$-CNTs (1.45 mF cm^{-2}). The high C$_{dl}$ value of NC@Fe$_2$O$_3$-CNTs is related to its three-dimensional sheet-like assembly structures with the high specific surface area that exposing more active sites and thus improve ORR activity [35].

In addition to the high activity, the long-term stability of ORR is also an important metric for the catalytic application.

Therefore, the ORR durability of both NC@Fe$_2$O$_3$-CNTs and 20 wt % Pt/C catalyst are investigated by chronoamperometry test at 0.6 V in O$_2$-saturated 0.1 M KOH solution with a rotation rate of 1600 rpm for 10 h. As shown in Fig. 4c, the NC@Fe$_2$O$_3$-CNTs catalyst maintained a higher and stable initial and final relative current than those of commercial Pt/C (20 wt %). Notably, the NC@Fe$_2$O$_3$-CNTs catalyst keeps ca. 82.9% of initial activity, which is significantly higher than that of the commercial Pt/C (20 wt %, retention ca. 65.9%) after 10 h. These results indicate that the NC@Fe$_2$O$_3$-CNTs catalyst has a better stability than commercial Pt/C, which could be ascribed to the unique core-shell structure along with a thick layer of N-doped carbon enveloped Fe$_2$O$_3$-CNTs composite. In contrast, Pt nanoparticles in commercial Pt/C is mainly loaded on the conductive carbon black surface, and they are easily exfoliated, aggregated, or poisoned during long-term stability test.
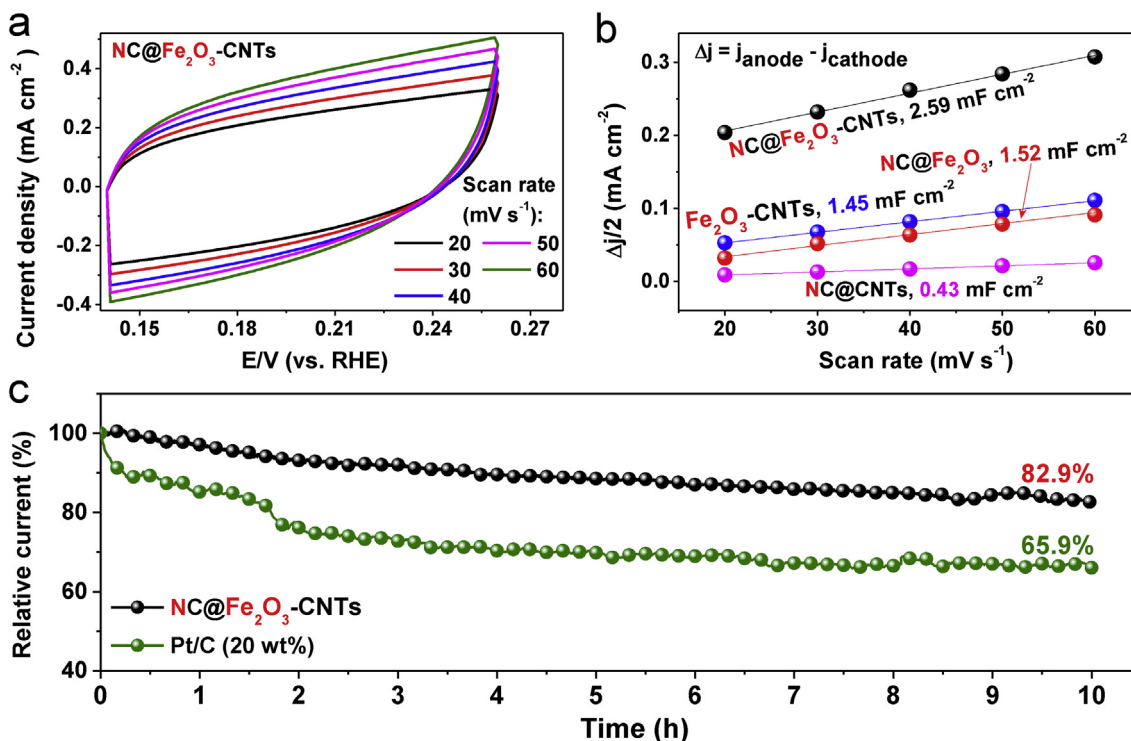
Fig. 4 – (a) Cyclic voltammograms (CV) in a potential window without faradaic processes of NC@Fe$_2$O$_3$-CNTs and (b) the summarized double-layer capacitance (C$_{dl}$) of different catalysts. (c) Chronoamperometric response of NC@Fe$_2$O$_3$-CNTs and Pt/C (20 wt %) catalysts at 0.60 V with a rotation speed of 1600 rpm for 10 h in O$_2$-saturated 0.1 M KOH.

Catalytic mechanism analysis

To further investigate the effects of elemental composition and chemical states of each element on catalytic activity, X-ray photoelectron spectroscopy (XPS) studies are performed. As expected, the NC@Fe$_2$O$_3$-CNTs exhibits a series of characteristic peaks in the survey spectrum, including C, N, O, and Fe elements, in which the high-resolution C 1s core level is deconvoluted into C=C (284.0 eV), C–C (284.8 eV), and C–O (286.0 eV) (Fig. S11) [36]. As shown in Fig. 5a, the N 1s core levels of all samples can be deconvoluted into four peaks corresponding to pyridinic-N (398.2 eV), pyrrolic-N (399.9 eV), graphitic-N (401.0 eV), and oxidized-N (403.7 eV), respectively (Fig. 5a) [37,38]. Previous studies have indicated that both pyridinic N, and graphitic N have direct contribution to ORR activity [39]. The XPS results show that the pyridinic N, pyrrolic N, and graphitic N are the main components in NC@Fe$_2$O$_3$-CNTs, NC@CNTs, and NC@Fe$_2$O$_3$. However, the graphitic N content is low in NC@CNTs, signifying the Fe$_2$O$_3$ contribution towards the formation of graphitic N. Therefore we concluded that the highest catalytic activity of NC@Fe$_2$O$_3$-CNTs among the other catalysts could be related to the high content of graphitic N. Moreover, one should note that the composition of N from the calcined product of polypyrrole is quite different from the structure of pure Fe–N$_4$ in iron porphyrin (Fig. S12).

The Fe 2p core levels of different catalysts are investigated, and each Fe 2p is split into two pairs of doublet and two satellite peaks (Fig. 5b). The binding energies at 710.6 and 723.8 eV are ascribed to Fe^{2+} species, the peaks at 713.6, and 726.8 eV are originated from Fe^{3+} species, and the rest of two peaks at 717.2 and 732.8 eV belong to satellite. Interestingly, the contents of Fe^{3+} in NC@Fe$_2$O$_3$-CNTs (49.4%) and NC@Fe$_2$O$_3$ (38.2%) are noticeably higher than that of Fe$_2$O$_3$-CNTs (24.1%), which indicates that the encapsulation of N-doped carbon protects the Fe^{3+} in a certain degree. Therefore, one can conclude that the Fe^{3+} may relate to the active site. In addition, the high-resolution O 1s core levels of all catalysts are deconvoluted into four peaks at binding energies of 530.1, 531.3, 532.2, and 533.3 eV, respectively. They are corresponding to the Fe–O, vacancies, C–O, and adsorbed H$_2$O/C=O (Fig. S13) [40]. High contents of oxygen vacancy are observed on both NC@Fe$_2$O$_3$-CNTs (29.5%) and NC@Fe$_2$O$_3$ (35.7%) due to the Fe$_2$O$_3$. The high content of oxygen vacancy promotes the H$_2$O molecule adsorption on Fe$_2$O$_3$ surface, which helps the Step III in Scheme 2. It should be noted that the microstructure of NC@Fe$_2$O$_3$-CNTs catalyst changed little after stability test (Fig. S14a), while the crystallinity of Fe$_2$O$_3$ in the catalyst was almost undetectable (Fig. S14b). In addition, one can find that the Fe 2p and N 1s XPS spectra of the catalyst also become very weak after stability test (Fig. S15). These results may be caused by a combination of catalyst exfoliation and electrolyte erosion over long time.

We proposed schematics of the possible catalytic mechanism according to the literature report and our experimental results. We concluded that the Fe–N$_4$ active site is crucial to the catalytic performance, while the Fe$_2$O$_3$ can enhance the adsorption of water molecules on the surface due to the high level of oxygen vacancy (Scheme 2). Step I: the dissolved O$_2$ molecule is adsorbed on the Fe–N$_4$ active site to form O$_2$*
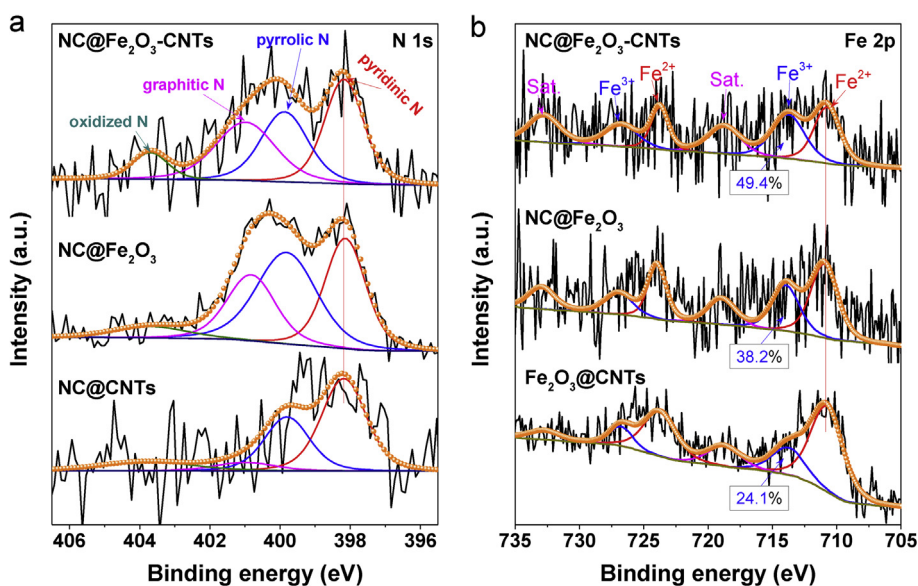
Fig. 5 — High-resolution XPS spectra of (a) N 1s regions of NC@Fe$_2$O$_3$-CNTs, NC@Fe$_2$O$_3$ and NC@CNTs, and (b) Fe 2p regions of NC@Fe$_2$O$_3$-CNTs, NC@Fe$_2$O$_3$ and Fe$_2$O$_3$-CNTs.
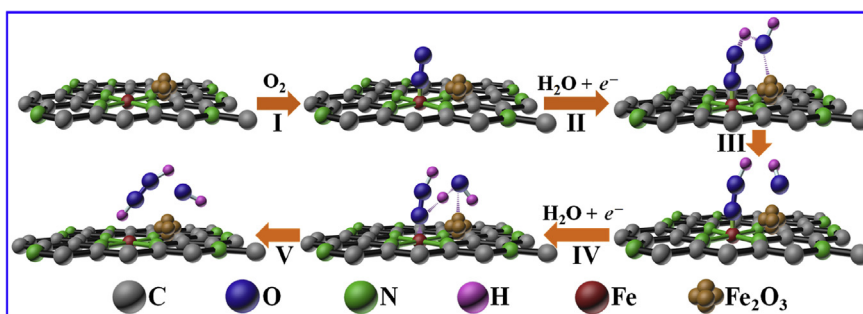
Scheme 2 — The proposed catalytic mechanism of NC@Fe$_2$O$_3$ catalyst for electrochemical O$_2$ reduction to H$_2$O$_2$ in alkaline medium.

($O_2 + {}^* \rightarrow O_2{}^*$) [41]. Step II: an intermediate state is formed between $O_2{}^*$ and adsorbed water on Fe$_2$O$_3$ by accepting one electron from the bulk ($O_2{}^* + H_2O + e^- \rightarrow OOH^* + OH^-$) [42]. Step III: H$^+$ moves to $O_2{}^*$ and OH$^-$ leaves from the surface. Step IV: a similar process as Step II happens and forms OOH* and H$_2$O intermediate ($OOH^* + H_2O + e^- \rightarrow H_2O_2 + OH^- + {}^*$). Step V: H$^+$ moves to $O_2{}^*$ and OH$^-$ leaves from the surface along with H$_2$O$_2$, and closes the catalytic cycle.

Conclusions

In summary, we developed a novel method of preparing polypyrrole-coated MIL-101-Fe-CNTs nanocomposite which was subsequently calcined at 800 °C in Ar to obtain three-dimensional NC@Fe$_2$O$_3$-CNTs. High-resolution TEM indicates that Fe$_2$O$_3$ in NC@Fe$_2$O$_3$-CNTs is a single crystal, which is different from literature reports on Fe-based ORR catalysts. Electrochemical studies revealed that the optimized NC@Fe$_2$O$_3$-CNTs exhibits a high ORR current density and a high selectivity towards H$_2$O$_2$ over a wide range of potential window as compared to those of controls. The K-L equation was used to evaluate the two-electron transfer feature, and the results are further confirmed by the RRDE. The XPS test also indicates that the pyridinic N, pyrrolic N, and Fe(III) species content alters the H$_2$O$_2$ selectivity. Furthermore, the graphitic N, oxygen vacancies and CNTs may promote the high current density.

Appendix A. Supplementary data

Supplementary data to this article can be found online at https://doi.org/10.1016/j.ijhydene.2019.12.187.

REFERENCES

[1] Zhou W, Gao J, Kou K, Meng X, Wang Y, Ding Y, Xu Y, Zhao H, Wu S, Qin Y. Highly efficient H_2O_2 electrogeneration from O_2 reduction by pulsed current: facilitated release of H_2O_2 from porous cathode to bulk. J Taiwan Inst Chem Eng. 2018;83:59—63.

[2] Liu Y, Quan X, Fan X, Wang H, Chen S. High-yield electrosynthesis of hydrogen peroxide from oxygen reduction by hierarchically porous carbon. Angew Chem Int Ed 2015;127:6941—5.

[3] Yi Y, Wang L, Li G, Guo H. A review on research progress in the direct synthesis of hydrogen peroxide from hydrogen and oxygen: noble-metal catalytic method, fuel-cell method and plasma method. Catal Sci Technol 2016;6:1593—610.

[4] Chen S, Chen Z, Siahrostami S, Kim TR, Nordlund D, Sokaras D, Nowak S, To JWF, Higgins D, Sinclair R, Nørskov JK, Jaramillo TF, Bao Z. Defective carbon-based materials for the electrochemical synthesis of hydrogen peroxide. ACS Sustain Chem Eng 2018;6:311—7.

[5] Lu Z, Chen G, Siahrostami S, Chen Z, Liu K, Xie J, Liao L, Wu T, Lin D, Liu Y, Jaramillo TF, Nørskov JK, Cui Y. High-efficiency oxygen reduction to hydrogen peroxide catalysed by oxidized carbon materials. Nat Catal 2018;1:156—62.

[6] Lee Y-H, Li F, Chang K-H, Hu C-C, Ohsaka T. Novel synthesis of N-doped porous carbons from collagen for electrocatalytic production of H_2O_2. Appl Catal B: Environ 2012;126:208—14.

[7] Chen Z, Chen S, Siahrostami S, Chakthranont P, Hahn C, Nordlund D, Dimosthenis S, Nørskov JK, Bao Z, Jaramillo TF. Development of a reactor with carbon catalysts for modular-scale, low-cost electrochemical generation of H_2O_2. React Chem Eng 2017;2:239—45.

[8] Fellinger T-P, Hasché F, Strasser P, Antonietti M. Mesoporous nitrogen-doped carbon for the electrocatalytic synthesis of hydrogen peroxide. J Am Chem Soc 2012;134:4072—5.

[9] Qiang Z, Chang J-H, Huang C-P. Electrochemical generation of hydrogen peroxide from dissolved oxygen in acidic solutions. Water Res 2002;36:85—94.

[10] Shen M, Wei C, Ai K, Lu L. Transition metal—nitrogen—carbon nanostructured catalysts for the oxygen reduction reaction: from mechanistic insights to structural optimization. Nano Res 2017;10:1449—70.

[11] Zhao Y, Lai Q, Wang Y, Zhu J, Liang Y. Interconnected hierarchically porous Fe, N-codoped carbon nanofibers as efficient oxygen reduction catalysts for Zn-air batteries. ACS Appl Mater Interfaces 2017;9:16178—86.

[12] Chen Y, Gokhale R, Serov A, Artyushkova K, Atanassov P. Novel highly active and selective Fe-N-C oxygen reduction electrocatalysts derived from in-situ polymerization pyrolysis. Nano Energy 2017;38:201—9.

[13] Iglesias D, Giuliani A, Melchionna M, Marchesan S, Criado A, Nasi L, Bevilacqua M, Tavagnacco C, Vizza F, Prato M, Fornasiero P. N-doped graphitized carbon nanohorns as a forefront electrocatalyst in highly selective O_2 reduction to H_2O_2. Chem 2018;4:106—23.

[14] Cui X, Xu Y, Chen L, Zhao M, Yang S, Wang Y. Ultrafine Pd nanoparticles supported on zeolite-templated mesocellular graphene network via framework aluminum mediation: an advanced oxygen reduction electrocatalyst. Appl Catal B: Environ 2019;244:957—64.

[15] Li J, Chen J, Wan H, Xiao J, Tang Y, Liu M, Wang H. Boosting oxygen reduction activity of Fe-N-C by partial copper substitution to iron in Al-air batteries. Appl Catal B: Environ 2019;242:209—17.

[16] Zhang Z, Sun J, Wang F, Dai L. Efficient oxygen reduction reaction (ORR) catalysts based on single iron atoms dispersed on a hierarchically structured porous carbon framework. Angew Chem Int Ed 2018;57:9038—43.

[17] Ye Y, Li H, Cai F, Yan C, Si R, Miao S, Li Y, Wang G, Bao X. Two-dimensional mesoporous carbon doped with Fe—N active sites for efficient oxygen reduction. ACS Catal 2017;7:7638—46.

[18] Guo J, Li Y, Cheng Y, Dai L, Xiang Z. Highly efficient oxygen reduction reaction electrocatalysts synthesized under nanospace confinement of metal—organic framework. ACS Nano 2017;11:8379—86.

[19] Xu X, Shi W, Li P, Ye S, Ye C, Ye H, Lu T, Zheng A, Zhu J, Xu L, Zhong M, Cao X. Facile fabrication of three-dimensional graphene and metal—organic framework composites and their derivatives for flexible all-solid-state supercapacitors. Chem Mater 2017;29:6058—65.

[20] Liu S, Wang Z, Zhou S, Yu F, Yu M, Chiang CY, Zhou W, Zhao J, Qiu J. Metal-organic-Framework-Derived hybrid carbon nanocages as a bifunctional electrocatalyst for oxygen reduction and evolution. Adv Mater 2017;29:1700874.

[21] Gao S, Fan B, Feng R, Ye C, Wei X, Liu J, Bu X. N-doped-carbon-coated Fe_3O_4 from metal-organic framework as efficient electrocatalyst for ORR. Nano Energy 2017;40:462—70.

[22] Raravikar NR, Keblinski P, Rao AM, Dresselhaus MS, Schadler LS, Ajayan PM. Temperature dependence of radial breathing mode Raman frequency of single-walled carbon nanotubes. Phys Rev B 2002;66:235424.

[23] Wei W, Ge H, Huang L, Kuang M, Al-Enizi AM, Zhang L, Zheng G. Hierarchically tubular nitrogen-doped carbon structures for oxygen reduction reaction. J Mater Chem A 2017;5:13634—8.

[24] Zhu Q-L, Xia W, Zheng L-R, Zou R, Liu Z, Xu Q. Atomically dispersed Fe/N-doped hierarchical carbon architectures derived from a metal—organic framework composite for extremely efficient electrocatalysis. ACS Energy Lett 2017;2:504—11.

[25] Zhang J, Dai L. Nitrogen, phosphorus, and fluorine tri-doped graphene as a multifunctional catalyst for self-powered electrochemical water splitting. Angew Chem Int Ed 2016;55:13296—300.

[26] Men B, Sun Y, Liu J, Tang Y, Chen Y, Wan P, Pan J. Synergistically enhanced electrocatalytic activity of sandwich-like N-doped graphene/carbon nanosheets decorated by Fe and S for oxygen reduction reaction. ACS Appl Mater Interfaces 2016;8:19533—41.

[27] Yang X, Zheng J, Zhen M, Meng X, Jiang F, Wang T, Shu C, Jiang L, Wang C. A linear molecule functionalized multi-walled carbon nanotubes with well dispersed PtRu nanoparticles for ethanol electro-oxidation. Appl Catal B: Environ 2012;121—122:57—64.

[28] Yang X, Wang X, Feng Y, Zhang G, Wang T, Song W, Shu C, Jiang L, Wang C. Removal of multifold heavy metal contaminations in drinking water by porous magnetic Fe_2O_3@AlO(OH) superstructure. J Mater Chem A 2013;1:473—7.

[29] Dorjgotov A, Ok J, Jeon Y, Yoon S-H, Shul YG. Activity and active sites of nitrogen-doped carbon nanotubes for oxygen reduction reaction. J ApplElectrochem 2013;43:387—97.

[30] Xu X, Zhong Z, Yan X, Kang L, Yao J. Cobalt layered double hydroxide nanosheets synthesized in water-methanol solution as oxygen evolution electrocatalysts. J Mater Chem A 2018;6:5999—6006.

[31] Zeng S, Lyu F, Nie H, Zhan Y, Bian H, Tian Y, Li Z, Wang A, Lu J, Li YY. Facile fabrication of N/S-doped carbon nanotubes with Fe_3O_4 nanocrystals enchased for lasting synergy as efficient oxygen reduction catalysts. J Mater Chem A 2017;5:13189—95.

[32] Wang Y, Zhu C, Feng S, Shi Q, Fu S, Du D, Zhang Q, Lin Y. Interconnected Fe, S, N-codoped hollow and porous carbon nanorods as efficient electrocatalysts for the oxygen reduction reaction. ACS Appl Mater Interfaces 2017;9:40298—306.

[33] Liu J, Sun X, Song P, Zhang Y, Xing W, Xu W. High-performance oxygen reduction electrocatalysts based on cheap carbon black, nitrogen, and trace iron. Adv Mater 2013;25:6879—83.

[34] Stevens MB, Enman LJ, Batchellor AS, Cosby MR, Vise AE, Trang CDM, Boettcher SW. Measurement techniques for the study of thin film heterogeneous water oxidation electrocatalysts. Chem Mater 2017;29:120—40.

[35] Li P, Zeng HC. Sandwich-like nanocomposite of CoNiO$_x$/reduced graphene oxide for enhanced electrocatalytic water oxidation. Adv Funct Mater 2017;27:1606325.

[36] Wang D, Liu S, Gan Q, Tian J, Isimjan TT, Yang X. Two-dimensional nickel hydroxide nanosheets with high-content of nickel(III) species towards superior urea electro-oxidation. J Electroanal Chem 2018;829:81—7.

[37] Peng X, Chen D, Yang X, Wang D, Li M, Tseng C-C, Panneerselvam R, Wang X, Hu W, Tian J, Zhao Y. Microwave-assisted synthesis of highly dispersed PtCu nanoparticles on three-dimensional nitrogen-doped graphene networks with remarkably enhanced methanol electrooxidation. ACS Appl Mater Interfaces 2016;8:33673—80.

[38] Zan Y, Zhang Z, Liu H, Dou M, Wang F. Nitrogen and phosphorus co-doped hierarchically porous carbons derived from cattle bones as efficient metal-free electrocatalysts for the oxygen reduction reaction. J Mater Chem A 2017;5:24329—34.

[39] Xia W, Mahmood A, Zou R, Xu Q. Metal—organic frameworks and their derived nanostructures for electrochemical energy storage and conversion. Energy Environ Sci 2015;8:1837—66.

[40] Zhang B, Wang L, Zhang Y, Ding Y, Bi Y. Ultrathin FeOOH nanolayers with abundant oxygen vacancies on BiVO$_4$ photoanodes for efficient water oxidation. Angew Chem Int Ed 2018;57:2248—52.

[41] Liu S, White MG, Liu P. Mechanism of oxygen reduction reaction on Pt(111) in alkaline solution: importance of chemisorbed water on surface. J Phys Chem C 2016;120:15288—98.

[42] Guo D, Shibuya R, Akiba C, Saji S, Kondo T, Nakamura J. Active sites of nitrogen-doped carbon materials for oxygen reduction reaction clarified using model catalysts. Science 2016;351:361—5.